

Adhesion-Enhanced Vertically Oriented Graphene on Titanium-Covered Quartz Glass toward High-Stability Light-Dimming-Related Applications

Fan Zhou, Bingyao Liu, Zhi Li, Jinghui Zhou, Junjie Shan, Lingzhi Cui, Jingyi Hu, Wenzhi Quan, Kejian Cui, Peng Gao, and Yanfeng Zhang*



Cite This: *ACS Nano* 2021, 15, 10514–10524



Read Online

ACCESS |



Metrics & More



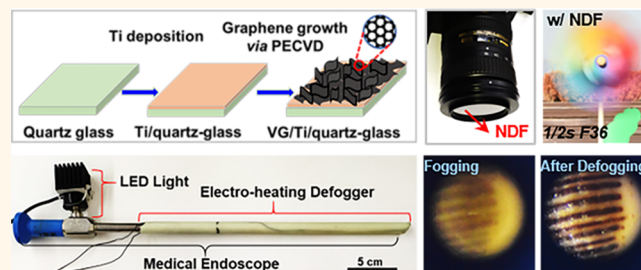
Article Recommendations



Supporting Information

ABSTRACT: Improving the adhesion property of graphene directly grown on an insulating substrate is essential for promoting the reliability and durability of the related applications. However, effective approaches have rarely been reported, especially for vertically oriented graphene (VG) films grown on insulating templates. To tackle this, we have developed a facile synthetic strategy by introducing an ultrathin (10 nm-thick) titanium (Ti) film on a quartz glass substrate as the adhesion layer, for plasma-enhanced chemical vapor deposition (PECVD) growth of VG films. This synthetic process induces the formation of Ti, oxygen (O), carbon (C)-containing adhesion layer (Ti (O, C)), offering improved interfacial adhesion due to the formation of chemical bonds among Ti and C atoms. Dramatically improved surface and interface stabilities have been achieved, with regard to its counterpart without a Ti adhesion layer. Moreover, we have also realized precise controls of the transparent/conductive property, surface roughness, and hydrophobicity, *etc.*, by varying the VG film growth time. We have also demonstrated the very intriguing application potentials of the hybrids in light-dimming related fields, that is, electro-heating defogging lenses and neutral density filters toward medical endoscope defogging and camera photography.

KEYWORDS: vertically oriented graphene nanowall film, plasma-enhanced chemical vapor deposition, titanium adhesion layer, medical endoscope electro-heating defogger, neutral density filter



Graphene has attracted tremendous research interests, owing to its excellent properties^{1–6} and broad-range applications in electronics,⁷ optoelectronics,^{8–11} sensors,¹² energy storage and conversions,^{13–15} *etc.* Particularly, direct growth of graphene on high-transparency glass *via* chemical vapor deposition (CVD) offers a graphene/glass hybrid, which can integrate the advantageous properties (transparency, conductivity, thickness-dependent light adsorption, *etc.*) of the two constituent materials,^{16–20} dramatically extending the application scenarios of graphene and glass.^{21–24}

Particularly, plasma-enhanced chemical vapor deposition (PECVD) enables the direct synthesis of graphene on low-softening-point glass (*e.g.*, soda-lime glass), under relative low growth temperature (*e.g.*, 500–600 °C).^{25,26} The resultant vertically oriented graphene (VG) nanosheet films present distinctive physical properties, for example, nest-like morphologies, enlarged specific surface area, abundant exposed sharp

edges, out-of-plane thermal and electrical conductivities, *etc.*^{27–29} Nevertheless, relatively poor electrical conductivity is usually inevitable, impeding the practical applications of VG/glass hybrids as transparent conductive materials. For tackling this dilemma, various synthetic strategies have recently been proposed to reduce the sheet resistances of VG nanowalls films grown directly on glass substrates,^{29,30} such as an ethanol-precursor-based PECVD route (on soda-lime glass at ~600 °C) for efficiently removing the amorphous carbons,²⁹ and a nitrogen doping process *via* a methane/acetonitrile-precursor-

Received: April 12, 2021

Accepted: May 24, 2021

Published: May 26, 2021



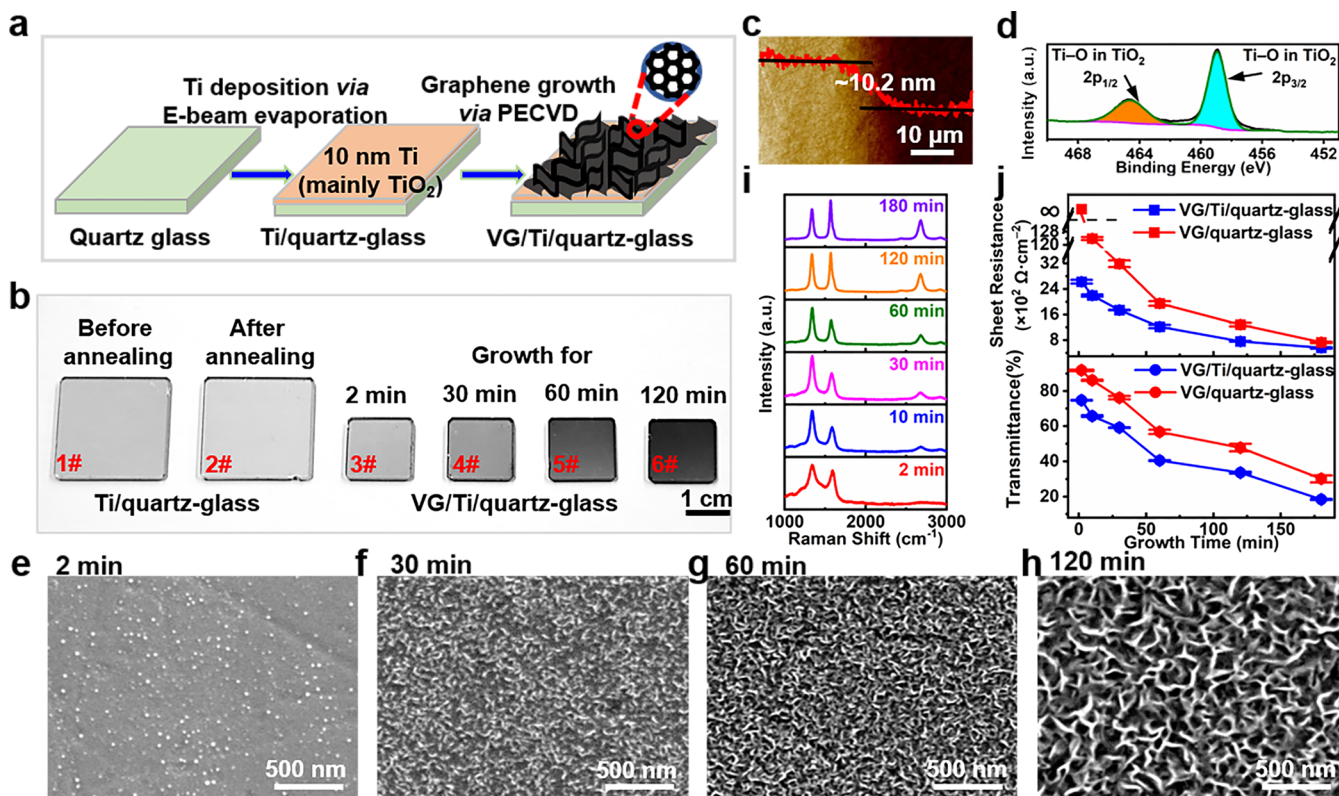


Figure 1. Controllable syntheses of VG nanowalls films on Ti/quartz-glass substrates (Ti thickness: ~ 10 nm) *via* PECVD. (a) Schematic diagram for the deposition of a Ti film on quartz glass and the PECVD growth of VG nanowall film on above. (b) Photographs of Ti/quartz-glass substrates before (sample 1) and after pregrowth annealing process (sample 2), and VG/Ti/quartz-glass samples grown for 2, 30, 60, and 120 min (samples 3–6), respectively. (c) AFM image of the transition regions from Ti/quartz-glass to bare quartz glass and the corresponding height profile. (d) XPS spectrum regarding Ti 2p for 10 nm Ti/quartz-glass substrate after annealing process. (e–h) Corresponding SEM images showing the surface morphologies of the hybrid samples. (i) Corresponding Raman spectra for the achieved samples in (b). (j) Growth-time-dependent transmittances and sheet resistances (bottom and top panels) of VG/Ti/quartz-glass and VG/quartz-glass samples, respectively. The data are the means (data points) and standard deviations (error bars) from 5 randomly selected positions on a specific sample. Growth parameters: H_2/CH_4 : 10/3 sccm; radio frequency power: ~ 300 W; growth temperature: ~ 700 °C.

based PECVD route (on high borosilicate glass at ~ 820 °C) for tailoring the carrier concentration.³⁰

In addition to enhancing the conductivity, improving the adhesion of graphene on functional insulating substrate is also crucial for various practical applications demanding robust stability and reliability.^{31,32} Generally, the interaction between graphene and insulating (or conductive) substrates mainly belongs to the van der Waals force type.^{31,33–35} This affords relatively poor interface adhesion, usually causing detachment or breakage of graphene films during the fabrication and working processes of graphene-based devices, leading to severe degradation in reliability and shortened service life.³⁶ It is hereby urgent to develop facile strategies to enhance the adhesion of directly grown graphene on insulating substrates, especially for the VG nanowall films with larger film thicknesses and surface corrugations.

Up to now, great endeavors have been made in enhancing the adhesion between transferred two-dimensional (2D) graphene films (CVD-grown graphene on Cu foils) and insulating substrates.^{36–38} Specifically, through a thermo-electrostatic bonding method, a nearly 3-fold increase (from ~ 0.65 to 1.81 J m^{-2}) in adhesion energy was achieved for graphene on the SiO_2/Si substrate.³⁶ Moreover, the adhesion energy of graphene on the SiO_x/Si substrate was also increased from ~ 2.98 to 10.09 and to 20.64 J m^{-2} , after rapid thermal annealing and vacuum annealing processes at ~ 450 °C,

respectively.³⁷ Ion beam bombardment of graphene on glass was also reported to increase the scratch resistance, that is, adhesion of graphene.³⁸ Unfortunately, these routes merely selected transferred graphene as targeted material, usually accompanied by obvious graphene quality degradation.^{37,38} So far, the adhesion-enhancement strategy for directly grown graphene on insulating substrates remains absent, let alone those for VG nanowalls films on glass.

In this work, an extremely thin (~ 10 nm) titanium (Ti) film will be innovatively introduced on the quartz glass template before PECVD growth (at ~ 700 °C) of VG films, which is proposed to serve as an adhesion layer for improving the interfacial adhesion property. Herein, the Ti element is selected by considering the following reasons. First, Ti–C chemical bonds are easy to form at the interface during the growth of carbon materials, according to the results for carbon nanotube growth on Ti layers.³⁹ This will induce enhanced adhesion of VG nanowalls films grown on Ti-film-decorated quartz glass (Ti/quartz-glass) substrates. Meanwhile, Ti and its oxides exhibit superior adhesion on various metals (Pt, Au, *etc.*) and dielectrics (SiO_2 and glass, *etc.*) through chemical interactions,^{40–43} ensuring their superior fastness on these substrates. Additionally, a transparent thin oxide layer (several to tens of nanometers) will evolve on the surface naturally once the Ti film is exposed to the air,^{44,45} thus affording relatively high transparency of the VG nanowall film on Ti/

quartz-glass (VG/Ti/quartz-glass) hybrid designed in this work. Altogether, this synthetic strategy will endow the derived hybrid with improved surface and interface stabilities (or interfacial adhesion), which is essential for promoting its versatile applications. Moreover, based on this transparent/conductive, light-attenuated and stable hybrid material, light-dimming-related applications will also be demonstrated for serving as electro-heating defogging lenses in medical endoscope defogging and neutral density filters (NDFs) for photography.

RESULTS AND DISCUSSION

To achieve this hybrid material, a PECVD route was selected for the direct growth of VG nanowalls on the deliberately designed Ti/quartz-glass substrate (Figure 1a). A 10 nm-thick Ti film was first deposited on quartz glass by using an electron beam (E-beam) evaporation technique, as characterized by atomic force microscope (AFM) (Figure 1c and supplementary Figure S1). Intriguingly, the ultrathin Ti film can be largely oxidized to transparent titanium dioxide (TiO_2) once the Ti/quartz-glass substrate is exposed to the air environment, as confirmed by X-ray photoelectron spectroscopy (XPS) (see Figure S2 for XPS spectrum regarding Ti 2p and corresponding analysis). This natural oxidation process can afford improved transparency of the Ti/quartz-glass substrate (sample 1 in Figure 1b; transmittance (T) to 550 nm light (the same hereinafter, unless stated otherwise): $\sim 69.0\%$). The advantages of Ti films over other metal (like Ni, Mo) films are also addressed by comparing their transparencies at the same metal film thickness (see supplementary Figure S3).

In prior graphene growth, the Ti/quartz-glass substrate experienced a two-step annealing process (at $\sim 300^\circ\text{C}$ for 2 h and then at $\sim 700^\circ\text{C}$ for 2 h; H_2 flow: 50 sccm) to remove the adsorbed contaminants (see Figure S4). As shown in the XPS spectrum regarding Ti 2p for the annealed 10 nm-Ti/quartz-glass substrate, only characteristic peaks of Ti–O in TiO_2 (~ 458.9 eV for Ti $2p_{3/2}$ and ~ 464.7 eV for Ti $2p_{1/2}$) are observed, according to a standard XPS database.⁴⁶ This means that the Ti film was thus further oxidized and nearly converted totally into TiO_2 after the deliberate annealing process (Figure 1d). An obvious increase in the transmittance of 10 nm-Ti/quartz-glass substrate from $\sim 69.0\%$ to 84.3% (before and after the annealing process) should be a more visual evidence of this Ti oxidation behavior (from sample 1 to sample 2, in Figure 1b). The residual oxygen existing in the PECVD system should participate in this oxidation process. Notably, the annealed Ti adhesion layer exhibits a rather flat surface morphology, followed with negligible dewetting behavior (Figure S5 and related discussion).

The Ti/quartz-glass substrate was then utilized as template for the PECVD growth of VG nanowalls. At a relatively low temperature of $\sim 700^\circ\text{C}$, abundant active carbon species (CH_x , C atoms and C_2H_x , etc.) were generated through the decomposition of a methane precursor with the aid of plasma, similar to the published references regarding VG films grown on SiO_2 ⁴⁷ and soda-lime glass.²⁶ Differently, some carbon (C) atoms diffused into the Ti film (converted to TiO_2 as confirmed above), substituted some of the oxygen (O) atoms, and even evolved into titanium oxycarbide (TiO_xC_y), which is analogous with that happening in carbothermal processes of TiO_2 nanoparticles⁴⁸ and nanotubes.⁴⁹ Meanwhile, other active carbon species adsorbed onto the substrate surface to form a carbon buffer layer instantly, on which nanometer-sized

graphene islands evolve. Some of these small graphene islands tend to curve upward to form VG nanosheet nuclei, followed by the migration of charged active carbon species and the fast growth of VG nanowalls.

Figure 1b shows the photographs of the PECVD-derived hybrids with growth times of 2, 30, 60, and 120 min (samples 3–6), respectively. The unannealed (sample 1) and annealed bare Ti/quartz-glass substrates (sample 2, before growth, defined as the hybrid grown for 0 min) are also displayed herein as references. Note that the light-attenuation abilities of PECVD-derived samples are gradually improved with increasing growth time, which can be further verified by ultraviolet–visible–near-infrared (UV–vis–NIR) transmittance spectra data (see Figure S6).

Surface morphology evolutions of corresponding PECVD-derived samples were then examined by scanning electron microscope (SEM), with growth times varying from 2, 30, 60 to 120 min (Figure 1e–h). The surface morphologies vary from sparsely distributed nanometer-sized dots (Figure 1e) and separated vertically oriented nanosheets (Figure 1f) to intertwined three-dimensional (3D) networks (Figure 1g,h), accompanied by increased nucleation density and nanosheet lateral size. Raman spectroscopy was then employed to identify the formation of VG nanowalls (Figure 1i). Three characteristic peaks typical for graphene, namely G peak ($\sim 1579\text{ cm}^{-1}$), D peak ($\sim 1340\text{ cm}^{-1}$), and 2D peak ($\sim 2680\text{ cm}^{-1}$) can be observed clearly, confirming the evolution of VG nanowalls on Ti/quartz-glass substrates. Specifically, after 2 min of growth, the Raman spectrum of the sample shows slightly merged D and G peaks as well as an unnoticeable 2D peak. This corresponds to the formation of an amorphous carbon buffer layer.⁵⁰ With extending growth times from 10, 30, 60, 120, to 180 min, the intensity ratios of D to G peaks ($I_{\text{D}}/I_{\text{G}}$) decrease from ~ 1.70 , 1.60, 1.49, 0.95, to 0.77, along with the increase of intensity ratios of 2D to D peaks ($I_{2\text{D}}/I_{\text{D}}$) from ~ 0.16 , 0.22, 0.37, 0.45, to ~ 0.49 (see Figure S7). This addresses the gradual increase of thickness and crystal quality of VG nanowalls films as PECVD growth time extends. Notably, this growth tendency agrees well with the PECVD growth of VG nanowalls films directly on soda-lime glass.^{26,29}

Figure 1j compares the transmittance and sheet resistance of the VG/Ti/quartz-glass and VG/quartz-glass samples synthesized under similar conditions (H_2/CH_4 : 10/3 standard cubic centimeter per minute (sccm); radio frequency power: ~ 300 W; growth temperature: $\sim 700^\circ\text{C}$) but with different growth times (2, 10, 30, 60, 120, and 180 min). With growth times increasing, the transmittances decrease from $\sim 74.7\%$, 65.8%, 59.1%, 40.4%, 33.6%, to 18.4% for the VG/Ti/quartz-glass hybrids and from $\sim 91.8\%$, 86.2%, 76.2%, 56.7%, 47.8%, to 30.0% for the VG/quartz-glass hybrids. Concomitantly, the sheet resistances also decrease from ~ 2.6 , 2.2, 1.7, 1.2, 0.8, to $0.6\text{ k}\Omega\text{ cm}^{-2}$ for VG/Ti/quartz-glass hybrids and from infinite ($>100\text{ k}\Omega\text{ cm}^{-2}$), ~ 12.4 , 3.2, 2.0, 1.3, to $0.7\text{ k}\Omega\text{ cm}^{-2}$ for VG/quartz-glass hybrids. Apparently, VG/Ti/quartz-glass hybrids present lower sheet resistances than those of Ti/quartz-glass samples under the identical growth time, accompanied by slightly reduced transmittances. This can be attributed to the introduction of a Ti adhesion layer and induced composition change into the Ti, O, C-containing (Ti (O, C)) layer, as induced by the preannealing of Ti/quartz-glass substrates and PECVD growth of VG films. Specifically, after 2 min of growth, the VG/quartz-glass hybrid shows a nonconductive nature (sheet resistance $>100\text{ k}\Omega\text{ cm}^{-2}$), while the VG/Ti/quartz-

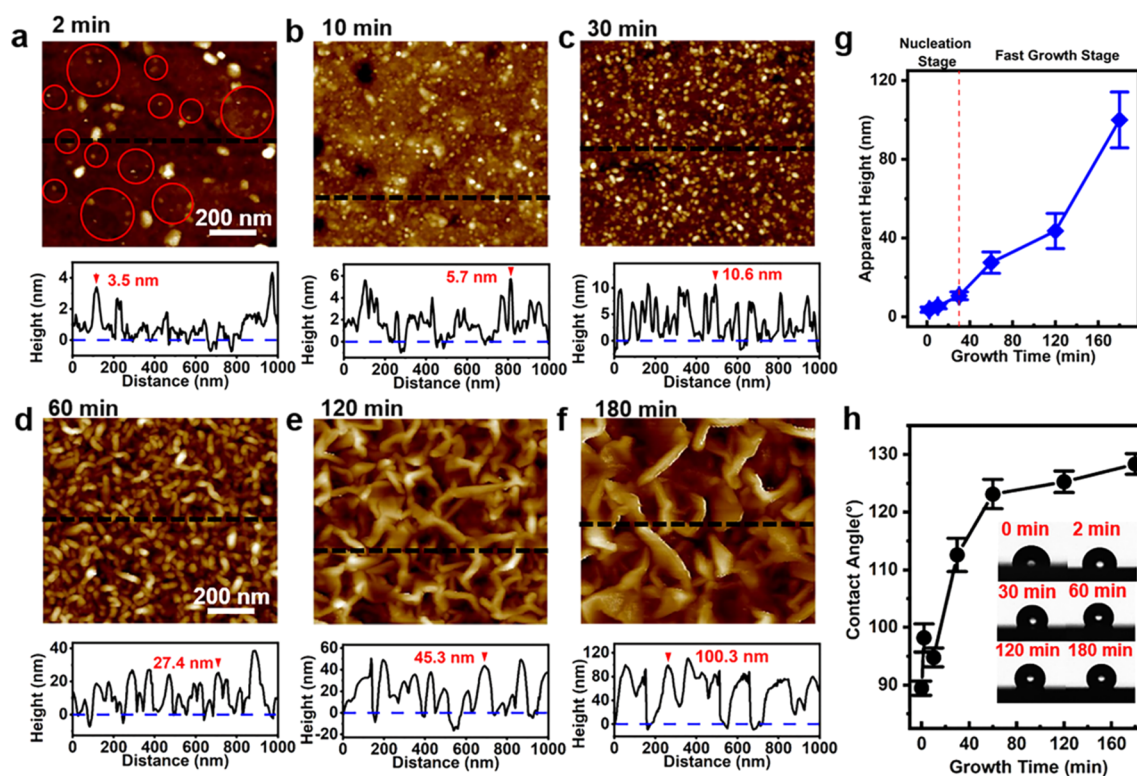


Figure 2. Growth morphology characterizations of VG nanowall films on Ti/quartz-glass substrates. (a–f) AFM images (top panel) and corresponding height profiles along the black dashed lines (bottom panels) of VG nanowall films on Ti/quartz-glass substrates grown for (a) 2, (b) 10, (c) 30, (d) 60, (e) 120, and (f) 180 min, respectively. The tiny VG nuclei in (a) are circled in red. (g–h) Statistics of apparent height and contact angle of the VG/Ti/quartz-glass hybrid as a function of growth time. Inset in (h): Photographs of contact angle data for VG/Ti/quartz-glass samples under various growth times. The statistics in (g) are derived from 50 height values collected from corresponding AFM images in (a–f) for each sample.

glass hybrid presents a sheet resistance of $\sim 2.6 \text{ k}\Omega \text{ cm}^{-2}$. This dramatic conductivity increase should arise from the fast formation of conductive TiO_xC_y components in the Ti (O, C) layer, as similarly reported for improving the conductivity of TiO_2 nanotubes by forming TiO_xC_y compounds (through carbothermal reduction).⁴⁹

To achieve an in-depth understanding of the growth behaviors of VG nanowall films on Ti/quartz-glass templates, surface morphology and apparent height evolutions with increasing growth time were further characterized by AFM (Figure 2a–g). Corresponding schematic diagrams for the growth processes of VG nanowall films are shown in Figure S8. Apparently, the whole growth process of the VG film can be separated into two stages, namely nucleation and fast growth stages (Figure 2g). At the first stage, a polycrystalline carbon buffer layer forms rapidly on the Ti/quartz-glass substrate, on which the nucleation of VG nanosheets initiates. Notably, at a growth time of 2 min, sparsely distributed, nanometer-sized VG nuclei are evolved to show an average apparent height of $\sim 3.6 \text{ nm}$ (small white dots circled in red in Figure 2a). The anomalously large white bumps should be the dropped carbon clusters from the inner wall of the quartz tube during annealing and/or VG growth processes. The VG nucleation density dramatically rises after 10 min growth (Figure 2b), accompanied by a slightly increased apparent height up to $\sim 4.9 \text{ nm}$.

As growth time extends to 30 min, the apparent height (from ~ 4.9 to 10.7 nm) and lateral size (from subten to tens of nanometers) of the VG nanosheets begin to rise sharply, along

with a gradual increase in the nucleation density (Figure 2c). The growth hereby enters the fast growth stage. After that, the VG nanowalls grow continuously to form intertwined 3D networks until touching with each other (Figure 2d–f). Correspondingly, the apparent heights increase from ~ 27.5 , 43.6 , to 100.0 nm with growth times increasing from 60, 120, to 180 min, respectively. At this time, some VG nanowalls grow so fast that they overwhelm the others, resulting in anomalously large VG nanowalls and enlarged intervals among them (Figure 2d–f). Figure 2g summarizes the apparent height evolutions of VG nanowalls films with growth time, as extracted from AFM characterization results. Briefly, these growth-time-dependent morphology and apparent height evolutions reflect the “nucleation–growth” mechanism of VG nanowalls films on the Ti/quartz-glass substrate.

Notably, the tunable surface morphologies of VG/Ti/quartz-glass hybrids endow them with variable surface-related properties, for example, hydrophobicity (Figure 2h). The contact angles present an increasing tendency (from $\sim 89.5^\circ$, 98.2° , 94.8° , 112.6° , 123.1° , 125.3° , to 128.4°) for the hybrids grown for 0, 2, 10, 30, 60, 120, and 180 min, respectively. Notably, the contact angle increases slowly and approaches an upper limit with growth time $>60 \text{ min}$, since the surface morphology shows more prominent 3D characteristics. Briefly, the VG/Ti/quartz-glass hybrids present a highly tunable hydrophobicity under different growth times, which should endow them with versatile applications especially in self-cleaning-related fields.^{25,51}

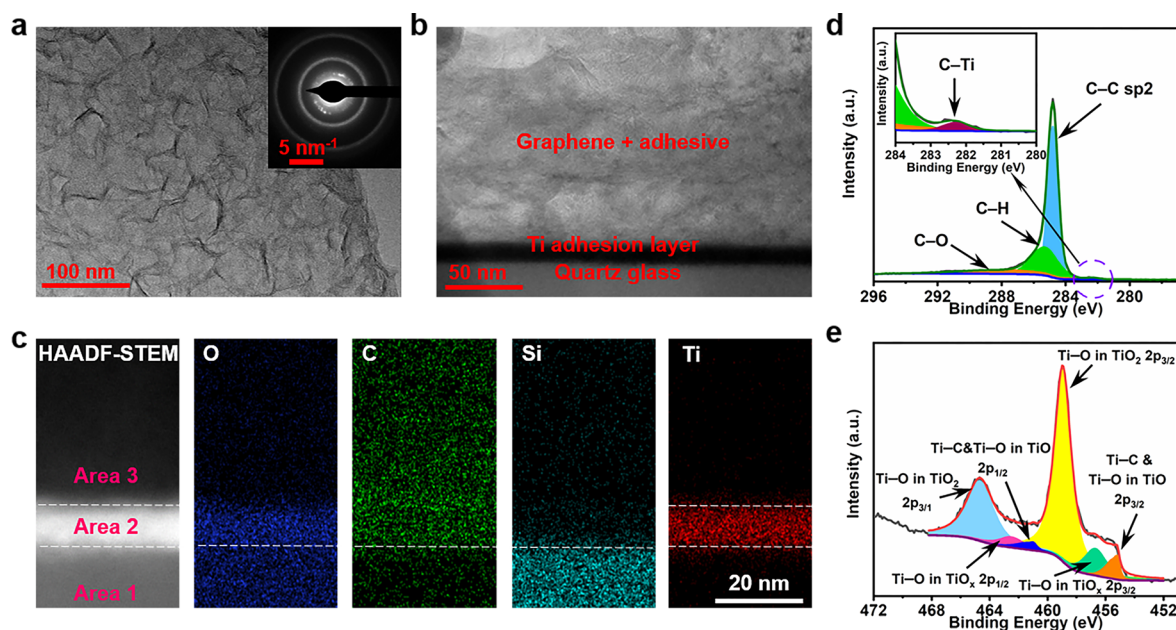


Figure 3. Microscopic structure and composition characterizations of VG/Ti/quartz-glass samples. (a) TEM image of VG films transferred from Ti/quartz-glass onto a TEM grid (VG film growth time: 60 min). Inset shows the corresponding SAED pattern recorded with a 200 nm scale aperture. (b) Cross-section TEM image of the VG/Ti/quartz-glass sample (VG film growth time: 120 min). (c) Cross-section HAADF-STEM image (leftmost) and corresponding EDS mappings regarding O, C, Si, and Ti elements of the VG/Ti/quartz-glass hybrid (VG film growth time: 120 min). The white dashed lines (in the different EDS images) circle the locations of the Ti (O, C) layer. The positions where EDS spectra were performed are labeled in magenta in the HAADF-STEM image. (d, e) XPS spectra regarding (d) C 1s and (e) Ti 2p for the VG/Ti/quartz-glass sample (VG film growth time: 40 min).

To investigate the microscopic structure, the as-grown VG nanowall films were then transferred from growth templates to transmission electron microscopy (TEM) grids for further characterizations (see [Methods](#) section for detailed transfer process). The low-magnification TEM image of a typical sample (VG film grown for 60 min, [Figure 3a](#)) shows a continuous film, on which numerous vertically oriented nanosheets (tens of nanometers in lateral size) stand. The corresponding energy dispersive spectroscopy (EDS) characterization enables the elemental analysis of the transferred sample (see [Figure S9](#) and corresponding analysis). Additionally, two legible diffraction rings typical for graphene can be noticed in the selected area electron diffraction (SAED) pattern (inset of [Figure 3a](#)), highly indicating the polycrystalline nature of the PECVD-derived VG nanowall film.

The introduction of a Ti (O, C) in-between layer in VG/Ti/quartz-glass hybrid should exert important influences on the interface properties. A cross-section TEM image was then utilized to unveil the interfacial sectional structure ([Figure 3b](#)) of the hybrid sample (VG film grown for 120 min). A well-defined lamellar structure can be clearly observed to encompass a 10 nm-thick Ti film sandwiched between the VG nanowall film and quartz glass. A high-angle annular dark-field scanning transmission electron microscopy (HAADF-STEM) image and corresponding EDS mappings regarding O, C, Si, and Ti elements were also obtained along the cross-section to determine the interface chemical composition ([Figure 3c](#)). Typical EDS spectra of different regions (with the concerned positions labeled in magenta in the HAADF-STEM image in [Figure 3c](#)) are also provided to determine the chemical compositions of these regions ([Figure S10](#)). Notably, uniformly distributed C and O elements are noticeable in the

Ti-rich region (circled by white dashed lines in [Figure 3c](#)), confirming the formation of a homogeneous Ti (O, C) layer.

Generally, bonding (physical and/or chemical bonding) between two materials dominates the adhesion of one onto the other. Chemical bonding usually contributes significantly to enhancing the interfacial adhesion.^{52,53} In this context, XPS characterizations were performed to achieve an elaborate analysis of the interfacial chemical bonding of VG/Ti/quartz-glass hybrid. The XPS spectrum regarding C 1s ([Figure 3d](#)) for a typical hybrid sample (VG film grown for 40 min) presents noticeable C(sp²)-C(sp²) (~284.8 eV) and C-H (~285.3 eV) peaks, accompanied by a broad C-O peak. These characteristic peaks are analogous with those of graphene grown on SiO₂⁵⁴ and glass⁵⁵ published previously and those of VG/quartz-glass sample grown for 40 min (herein as a reference), but with other parameters maintained (see [Figure S11](#) for corresponding XPS spectrum regarding C 1s). Distinctively, an extra C-Ti peak also appears at ~282.3 eV (inset of [Figure 3d](#)), according to XPS data for Ti-containing diamond-like carbon films.⁵⁶ Altogether, the current XPS data unambiguously manifest the formation of Ti-C chemical bonds in the Ti (O, C) layer and at the interface.

Correspondingly, in the XPS spectrum regarding Ti 2p, a couple of unsymmetrical Ti-C and Ti-O (in TiO) peaks also occur, that is, ~455.2 eV for Ti 2p_{3/2} and ~461.0 eV for Ti 2p_{1/2} ([Figure 3e](#)). Besides, two groups of symmetrical peaks appear to show the formation of Ti-O bonds in TiO₂ (~459.0 eV for Ti 2p_{3/2} and ~464.7 eV for Ti 2p_{1/2}) and TiO_x (~456.7 eV for Ti 2p_{3/2} and ~462.5 eV for Ti 2p_{1/2}), respectively. These characteristic peak positions agree well with those regarding carbothermal-synthesized TiO_xC_y⁴⁸ and titanium/organics interfaces.⁵⁷ Altogether, a Ti (O, C) transition area should evolve to vary from C-rich to Ti-rich

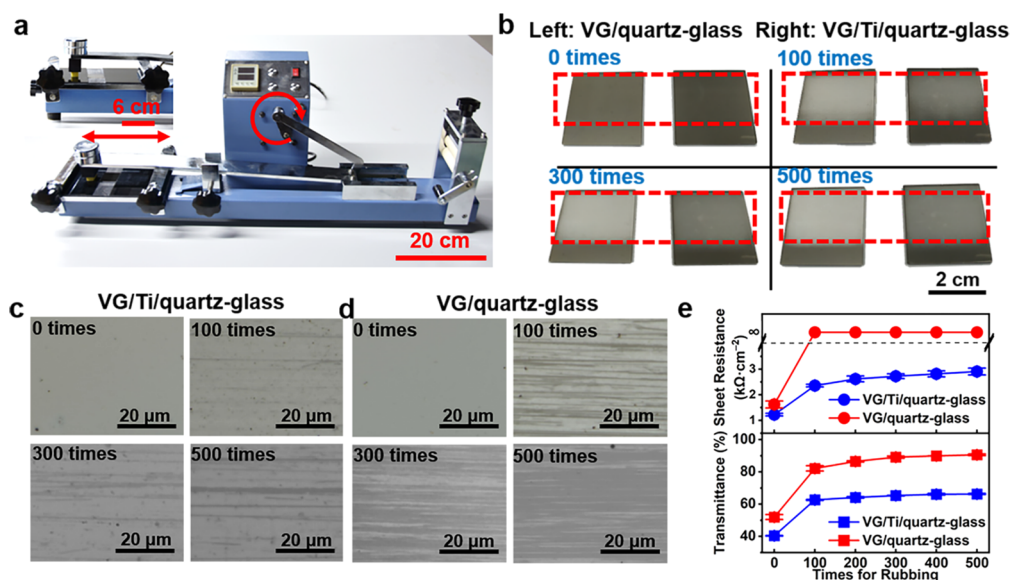


Figure 4. Adhesion property evaluations of VG nanowalls films grown on Ti/quartz-glass and quartz-glass substrates (VG film growth time: 60 min). (a) Photograph of homemade adhesion tester (refitted from a YS71 rubbing color fastness tester). The red arrows denote the rotation or translational movement directions of the components. Motions of the sample relative to the friction head along the red straight arrow direction are restricted by the groove (depth: ~ 1 mm) on the black acrylic plate. The normal force applied to the eraser friction head is fixed to ~ 9 N. Inset in (a): the zoom-in images of the regions where the samples are rubbed (horizontal size: ~ 30 mm \times 30 mm; thickness: ~ 1 mm). (b) Photographs of VG/quartz-glass (left in each panel) and VG/Ti/quartz-glass (right in each panel) hybrids before and after rubbed for 100 (top left to top right), 300 (bottom left), and 500 times (bottom right panel). (c, d) OM images of the two types of samples shown in (b). (e) Transmittances and sheet resistances for the two types of samples as a function of rubbing time.

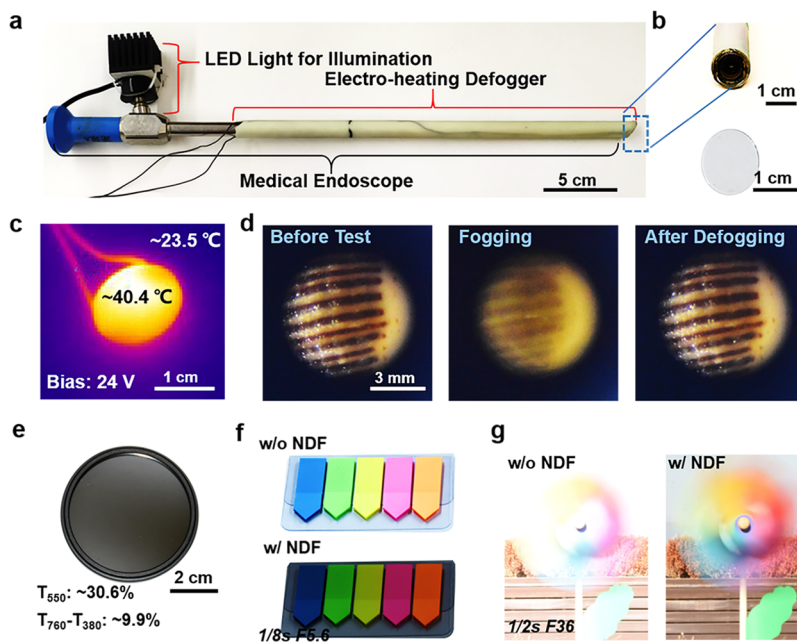


Figure 5. Light-dimming-related applications of VG/Ti/quartz-glass hybrids as transparent electro-heating defogging lenses for medical endoscope defogging and as NDFs for camera photography. (a) Photograph of the medical endoscope equipped with a LED light for illumination and an electro-heating defogger using the VG/Ti/quartz-glass hybrid as defogging lens. (b) Top panel: Zoom-in image of the transparent electrical-heating defogging lens. Bottom panel: Photograph of the VG/Ti/quartz-glass sample (VG film growth time: 2 min; transmittance: $\sim 73.1\%$; sheet resistance: ~ 4.5 $k\Omega \cdot cm^{-2}$) used for defogger fabrication. (c) Infrared thermal image of the hybrid sample at the steady heating state under a 24 V bias. Silver paste was deposited at both ends of the sample as electrodes. (d) Optical images of textures on a shell observed through the medical endoscope shown in (a) before defogging test, in fogged state, and after defogging process (left, middle, and right panels), respectively. (e) Photograph of the VG/Ti/quartz-glass hybrid-based NDF (VG film growth time: 120 min). (f) Photographs of tags with different colors taken with (bottom panel) and without the NDF (top panel) shown in (e), with exposure time of $1/8$ s and aperture size of F5.6. (g) Long-exposure photographs of a rotating chromatic windmill toy taken with (right panel) and without the designed NDF (left panel) shown in (e), with an exposure time of $1/2$ s and aperture size of F36.

regions (from surface to inner surface regions), accompanied by Ti–C chemical bonds formation. This Ti (O, C) transition layer affords relatively strong adhesion of VG films on Ti/quartz-glass substrates, with regard to that of VG films on quartz-glass substrates.

To reasonably evaluate the adhesion of VG nanowalls films on Ti/quartz-glass and bare quartz-glass substrates, a home-made adhesion tester was designed (Figure 4a). More details are presented in Figure S12 and the related descriptions in the Supporting Information. With this setup, the adhesion property can be roughly evaluated by automatically rubbing the samples for a certain number of times (Video S1) and then analyzing their surface damages. Photographs of the two types samples after rubbed for 0 (before rubbed), 100, 300, and 500 times are displayed in Figure 4b. Surprisingly, variations in color contrasts between rubbed and unrubbed regions are less obvious for the VG/Ti/quartz-glass hybrids, possibly due to more intense interfacial interaction between VG films and Ti/quartz-glass substrates. In contrast, the rubbed regions on VG/quartz-glass samples present much lighter color contrasts than those of the unrubbed regions, indicating severe removal of the VG films after the rubbing processes. Raman spectrum evolutions also reveal the gradual removal of VG films as the time of rubbing increases (Figure S13).

Corresponding optical microscope (OM) images of the VG/Ti/quartz-glass (Figure 4c) and VG/quartz-glass samples (Figure 4d) undergoing different times of rubbing provide clear evidence of the surface morphology evolutions on a micrometer-scale. Notably, after rubbing treatments for 100, 300, and 500 times, only a few rubbing-caused stripe-like scratches (ribbons with darker color contrasts in Figures 4c,d) appear on VG/Ti/quartz-glass sample surface (Figure 4c). The scratches merely occupy a small portion of the sample surface even after a 500-time rubbing treatment. In contrast, more scratches occur on the VG/quartz-glass sample surface just after the 100-time rubbing process. To make things worse, the scratches nearly cover the whole VG/quartz-glass surface (Figure 4d) with the rubbing times approaching 500.

To further evaluate the effect of rubbing, transmittance and sheet resistance values of VG/Ti/quartz-glass and VG/quartz-glass samples after different times of rubbing were also collected (Figure 4e). After a 100-time rubbing treatment, the VG/quartz-glass sample shows infinite sheet resistance, along with increased transmittance from ~52.0% to 82.2%. In comparison, the VG/Ti/quartz-glass sample merely exhibits a certain increase in sheet resistance (from ~1.2 to 2.4 $\text{k}\Omega \text{ cm}^{-2}$), along with transmittance rising from ~40.4% to 62.7% accordingly. Moreover, only a slight increase in transmittance (from ~62.9% to 66.3%) and sheet resistance (from ~2.4 to 2.9 $\text{k}\Omega \text{ cm}^{-2}$) happens in the VG/Ti/quartz-glass hybrid, as the times of rubbing extend from 100 to 500. In this regard, the VG/Ti/quartz-glass hybrids exhibit much better resistances against mechanical damage, hereby possessing superior surface and interface stabilities than those of the VG/quartz-glass hybrid.

Considering the transparent/conductive property and nearly wavelength-independent light attenuation property in visible spectrum range (see UV–vis–NIR spectra in Figure S6), the VG/Ti/quartz-glass hybrid, featured with relatively high surface and interface stability, is expected to find broad-range applications in various light-dimming-related fields. Herein, the applications such as transparent electro-heating defogging lens

for medical endoscope and as neutral density filter (NDF) for photography are elaborately demonstrated (Figure 5).

Medical endoscopes are nearly indispensable in surgery to monitor lesions hidden in body or organ cavities that are difficult to detect through routine approaches. However, owing to the relatively high humidity in cavities and cool surface of the medical endoscope lens when it is dipped into the cavity, the lens is usually fogged. This usually leads to a blurred scene in the working state, and efficient defogging is highly desired for this application scenario to achieve clear imaging. Indium tin oxide (ITO), a commonly used transparent conductive material, suffers from an obvious increase in electrical resistance (by ~130%) after the long-time high-temperature annealing treatment (~100 °C, 30 days, in air),⁵⁸ thus not suitable to be utilized as the electro-heating defogging lens that demands rigorous repetitive sterilization processes, that is, >120 °C and high relative humidity. In contrast, considering its superior chemical and thermal stabilities, graphene should serve as an ideal electro-heating film for medical endoscope defogging applications.

Herein, an electro-heating defogger was fabricated by using VG/Ti/quartz-glass hybrids as defogging lens for medical endoscope defogging (Figure 5a,b, more details in the Methods section and Figure S14). A light emitting diode (LED) light is used for illumination. Notably, by applying a secure voltage of 24 V, the surface temperature of the defogger was stabilized at ~40.4 °C, a safe temperature to tissues, as shown in the infrared thermal image (Figure 5c). Subsequently, the defogging performance was carefully examined with the designed equipment that simulated the working environment of an endoscope (Figure S15). Before the defogger was fogged, the textures on shells can be clearly seen through the endoscope (left panel of Figure 5d). When the relative humidity in the dark chamber rose to ~90%, the defogging lens was instantly fogged once inserted into the dark chamber (middle panel of Figure 5d). By applying a 24 V bias, the fog started to vanish, and the defogging process was finished within 40 s (Video S2), leading to the reappearance of a clear image for textures on shells (right panel of Figure 5d). This indicates the superb defogging ability of the electro-heating defogger. Additionally, such a defogging lens also shows high defogging robustness and biocompatibility comparable to that of bare endoscope lens (Figures S14 and S16 and related discussion), thus presenting promising applications for recyclable clinical medical endoscopes.

Furthermore, an NDF was also fabricated based on the VG/Ti/quartz-glass hybrid and installed on the camera lens for photography tests (Figure 5e, more details in Methods section). When the tags with different colors are photographed (aperture: F5.6; exposure time: 1/8 s), the picture taken with the NDF presents homogeneously attenuated brightness for all colors (bottom panel in Figure 5f), compared with that taken without NDF (top panel in Figure 5f). This confirms the nearly color-nonspecific light attenuation ability of the NDF. After that, the overexposure-mitigated capability of the NDF was also examined in long-exposure photography of a rotating chromatic toy windmill (Figure 5g), by using a small aperture (F36) and an extended exposure time (1/2 s). Trails of rotating windmill blades in various colors can be recorded in one photograph, generating a fascinating motion-blurred effect in the obtained long-exposure photograph. Notably, severe overexposure phenomenon occurs in the picture taken without the designed NDF (left panel of Figure 5g). Herein, the

overexposure effect can be effectively eliminated when a NDF was utilized (right panel of Figure Sg). Altogether, such VG/Ti/quartz-glass hybrid based NDF exhibits tantalizing application potentials in various light-attenuation products, such as goggles, sunglasses, and precise optical elements. Moreover, by virtue of the Ti-adhesion-layer technique, VG nanowall films can be directly synthesized on various functional substrates, featured with dramatically enhanced interfacial adhesion. This will dramatically extend their applications to more versatile fields, such as solar cells, electrochemical cell electrodes, and gas sensors, which should possess much improved stabilities and prolonged service lifetimes.

CONCLUSIONS

In summary, a facile synthetic strategy has been developed for enhancing the adhesion of PECVD-derived VG nanowall films on quartz glass templates, by introducing an in-between Ti film as the adhesion layer to induce the formation of Ti–C chemical bonds at the interface. VG/Ti/quartz-glass hybrids with highly tunable properties are achieved through precisely tailoring the growth time of VG films. The adhesion of VG films on Ti/quartz-glass substrate is dramatically enhanced with regard to that on a bare quartz-glass template. Based on the transparent/conductive properties and nearly wavelength-independent light attenuation ability for visible light, this highly stable hybrid material is utilized to develop a broad range of applications, for example, electro-heating defogging lenses for medical endoscopes and NDFs for proper exposure photography. This work thereby provides a broader insight into the direct synthesis of high-quality 2D materials on functional insulating substrates, especially from the viewpoint of improving the interface adhesion property and promoting their daily life-related applications in various fields.

METHODS

Syntheses of VG/Ti/Quartz-Glass and VG/Quartz-Glass Hybrids. Quartz glass pieces (horizontal size: 15 mm × 15 mm, 25 mm × 25 mm, 30 mm × 30 mm; thickness: 1 mm) were ultrasonically cleaned in deionized water, acetone, and isopropanol, successively, and then dried in blowing nitrogen gas. To achieve the VG/Ti/quartz-glass (VG/quartz-glass) hybrid, the Ti/quartz-glass (bare quartz glass) substrate was utilized as a template for VG film growth, which was achieved through E-beam evaporation of Ti film on quartz glass. A quartz tube (diameter: 3 in.) was mounted in the three-zone tube furnace (Thermo Scientific, Lindberg) to serve as the reaction chamber. Copper coils that were connected to a radio frequency power supply (Zhongshan K-mate Electronics Co. Ltd., HERO-300W) surrounded the quartz tube near the inlet end for plasma generation. The substrates placed on a quartz slab were positioned at the center of first temperature zone of the furnace, ~40 cm away from the copper coil. The quartz tube was pumped to the lowest vacuum by a mechanical vacuum pump (KYKY Technology Co. Ltd., RVD-4) for system cleanness, followed by a two-step annealing process (300 °C for 2 h and then 700 °C for 2 h) under a gas flow of 50 sccm H₂ for removal of adsorbed contaminants. During the VG film growth process, a mixture gas flow of 10 sccm H₂ and 3 sccm CH₄ was introduced into the quartz tube under the temperature of ~700 °C, and the plasma generating power supply was turned on, whose power was set as 300 W. After VG film growth, the CH₄ flow was cut off, and the radio frequency power supply was switched off. The furnace was cooled down in a gas flow of 20 sccm H₂.

Transfer of VG Nanowall Films. The VG film was transferred onto the TEM grid for TEM characterization through a poly(methyl methacrylate) (PMMA)-assisted transfer process. A thin PMMA (AR-P 679.04) film was first spin-coated onto the VG/Ti/quartz glass

sample (speed for spin-coating: ~1000 rpm for 10 s and then ~2800 rpm for 60 s). Subsequently, the PMMA-coated sample was baked at ~120 °C for 10 min to solidify the PMMA film, and then the substrate was etched away in hydrofluoric acid solution (volume ratio of hydrofluoric acid to water: ~1:2). After that, the PMMA-coated VG film was then rinsed in deionized water for 5 times, dried by the infrared lamp illumination for 30 min, and then collected onto the TEM copper grid. The PMMA film was finally removed through soaking the TEM grid in acetone (AR-P) overnight.

Characterizations. The samples were characterized by Raman spectroscopy (Horiba, LabRAM HR Evolution; 532 nm laser excitation), transmittance meter (Shenzhen Speedre Technology Co. Ltd., SDR851), four-probe resistance-measuring meter (Guangzhou 4-probe Tech Co. Ltd., RTS-4), UV–vis–NIR spectrometer (PerkinElmer Lambda 950), SEM (FEI Quattro S; operating at 20 kV), AFM (BRUKER Dimension Icon; working at the tapping mode), contact angle system (DataPhysics, OCA20), XPS (Kratos Analytical Axis-Ultra spectrometer using a monochromatic Al K α X-ray source), TEM (FET Tecnai F20; operated at 200 kV), aberration-corrected STEM (FEI Titan Cubed Themis G2 300; operated at 300 kV) for HAADF images and EDS mappings, optical microscope (Nikon, Eclipse LV100ND), and infrared thermometer (FLIR A6) for infrared images.

Fabrication of VG/Ti/Quartz-Glass Hybrid-Based NDF. A VG/Ti/quartz-glass round piece (diameter: ~52 mm; thickness: ~1 mm; VG film growth time: 120 min) was fixed into a filter adapter with proper size to achieve the NDF. The derived NDF was then equipped in front of the digital camera (Nikon, 7200) lens for light attenuation in photography.

Fabrication of Electro-Heating Defogger by Using VG/Ti/Quartz-Glass Hybrid as Defogging Lens. To achieved electro-heating defogger, a VG/Ti/quartz-glass oval piece (long axis: ~13 mm; short axis: ~11 mm; growth time: 2 min) was printed with Ag electrodes at both its ends and then stuck on the beveled end of a sleeve with sealants as the defogging lens. After that, the electro-heating defogger was equipped on the medical endoscope, with connection wires toward the power source hidden inside the sleeve.

ASSOCIATED CONTENT

Supporting Information

The Supporting Information is available free of charge at <https://pubs.acs.org/doi/10.1021/acsnano.1c03063>.

Video S1: Work process of the homemade adhesion tester as the VG/Ti/quartz-glass sample is rubbed (MP4)

Photograph of the bare Ti/quartz-glass substrate used for Ti thickness evaluation, supplementary XPS spectra of Ti/quartz-glass substrates, light transmittance characterizations of various 10 nm-thick metal (Ti, Ni and Mo) films on quartz glass, schematic of the growth procedure of the VG nanowall film, further discussion regarding the Ti/quartz-glass substrates, UV–vis–NIR transmittance spectra of Ti/quartz-glass substrates (before and after annealing) and VG/Ti/quartz-glass hybrids under different growth time, Raman I_D/I_G and I_{2D}/I_G values extracted from Raman spectra as a function of VG growth time, schematics for VG nanowalls films grown on Ti/quartz-glass substrates, EDS characterization of the transferred VG nanowalls film, supplementary EDS characterization of the cross-section STEM sample, XPS spectrum regarding C 1s of the VG/quartz-glass sample (growth time: 40 min), photographs of some key components on the homemade adhesion tester, rubbing time-dependent Raman spectra of the VG/Ti/quartz-glass and VG/quartz-glass samples (growth time: 60 min), the fabrication schematic of the electro-heating

defogger and related discussion about its biocompatibility, photograph of the setup used for defogging performance evaluation, cyclical performance characterization of the defogging lens, and details about the construction and work processes of the homemade adhesion tester (PDF)

Video S2: Defogging process of the electro-heating defogger (MP4)

AUTHOR INFORMATION

Corresponding Author

Yanfeng Zhang – School of Materials Science and Engineering, Peking University, Beijing 100871, P.R. China; Beijing Graphene Institute (BGI), Beijing 100095, P.R. China; orcid.org/0000-0003-1319-3270; Email: yanfengzhang@pku.edu.cn

Authors

Fan Zhou – Academy for Advanced Interdisciplinary Studies, Peking University, Beijing 100871, P.R. China; School of Materials Science and Engineering, Peking University, Beijing 100871, P.R. China

Bingyao Liu – Academy for Advanced Interdisciplinary Studies, Peking University, Beijing 100871, P.R. China; Electron Microscopy Laboratory and International Center for Quantum Materials, School of Physics, Peking University, Beijing 100871, P.R. China

Zhi Li – Beijing Graphene Institute (BGI), Beijing 100095, P.R. China

Jinghui Zhou – Beijing Graphene Institute (BGI), Beijing 100095, P.R. China

Junjie Shan – Beijing Graphene Institute (BGI), Beijing 100095, P.R. China

Lingzhi Cui – Beijing Graphene Institute (BGI), Beijing 100095, P.R. China

Jingyi Hu – Academy for Advanced Interdisciplinary Studies, Peking University, Beijing 100871, P.R. China; School of Materials Science and Engineering, Peking University, Beijing 100871, P.R. China

Wenzhi Quan – Academy for Advanced Interdisciplinary Studies, Peking University, Beijing 100871, P.R. China; School of Materials Science and Engineering, Peking University, Beijing 100871, P.R. China

Kejian Cui – Beijing Graphene Institute (BGI), Beijing 100095, P.R. China

Peng Gao – Electron Microscopy Laboratory and International Center for Quantum Materials, School of Physics, Peking University, Beijing 100871, P.R. China; Beijing Graphene Institute (BGI), Beijing 100095, P.R. China; Collaborative Innovation Center of Quantum Matter, Beijing 100871, P.R. China; orcid.org/0000-0003-0860-5525

Complete contact information is available at: <https://pubs.acs.org/10.1021/acsnano.1c03063>

Notes

The authors declare no competing financial interest.

ACKNOWLEDGMENTS

This work was financially supported by the National Basic Research Program of China (no. 2016YFA0200103), the National Natural Science Foundation of China (nos.

51925201, 51520105003, and 52021006), Beijing Municipal Natural Science Foundation (no. 2214085), and Beijing Municipal Science and Technology Commission Project (no. Z201100008720001).

REFERENCES

- (1) Novoselov, K. S.; Geim, A. K.; Morozov, S. V.; Jiang, D.; Katsnelson, M. I.; Grigorieva, I. V.; Dubonos, S. V.; Firsov, A. A. Two-Dimensional Gas of Massless Dirac Fermions in Graphene. *Nature* **2005**, *438*, 197–200.
- (2) Balandin, A. A.; Ghosh, S.; Bao, W.; Calizo, I.; Teweldebrhan, D.; Miao, F.; Lau, C. N. Superior Thermal Conductivity of Single-Layer Graphene. *Nano Lett.* **2008**, *8*, 902–907.
- (3) Chen, J.-H.; Jang, C.; Xiao, S.; Ishigami, M.; Fuhrer, M. S. Intrinsic and Extrinsic Performance Limits of Graphene Devices on SiO₂. *Nat. Nanotechnol.* **2008**, *3*, 206–209.
- (4) Du, X.; Skachko, I.; Barker, A.; Andrei, E. Y. Approaching Ballistic Transport in Suspended Graphene. *Nat. Nanotechnol.* **2008**, *3*, 491–495.
- (5) Lee, C.; Wei, X.; Kysar, J. W.; Hone, J. Measurement of the Elastic Properties and Intrinsic Strength of Monolayer Graphene. *Science* **2008**, *321*, 385–388.
- (6) Nair, R. R.; Blake, P.; Grigorenko, A. N.; Novoselov, K. S.; Booth, T. J.; Stauber, T.; Peres, N. M. R.; Geim, A. K. Fine Structure Constant Defines Visual Transparency of Graphene. *Science* **2008**, *320*, 1308–1308.
- (7) Lin, Y.-M.; Valdes-Garcia, A.; Han, S.-J.; Farmer, D. B.; Meric, I.; Sun, Y.; Wu, Y.; Dimitrakopoulos, C.; Grill, A.; Avouris, P.; Jenkins, K. A. Wafer-Scale Graphene Integrated Circuit. *Science* **2011**, *332*, 1294–1297.
- (8) Park, J.; Ahn, Y. H.; Ruiz-Vargas, C. Imaging of Photocurrent Generation and Collection in Single-Layer Graphene. *Nano Lett.* **2009**, *9*, 1742–1746.
- (9) Xia, F.; Mueller, T.; Lin, Y.-m.; Valdes-Garcia, A.; Avouris, P. Ultrafast Graphene Photodetector. *Nat. Nanotechnol.* **2009**, *4*, 839–843.
- (10) Bonaccorso, F.; Sun, Z.; Hasan, T.; Ferrari, A. C. Graphene Photonics and Optoelectronics. *Nat. Photonics* **2010**, *4*, 611–622.
- (11) Koppens, F. H. L.; Mueller, T.; Avouris, P.; Ferrari, A. C.; Vitiello, M. S.; Polini, M. Photodetectors Based on Graphene, Other Two-Dimensional Materials and Hybrid Systems. *Nat. Nanotechnol.* **2014**, *9*, 780–793.
- (12) Shao, Y.; Wang, J.; Wu, H.; Liu, J.; Aksay, I. A.; Lin, Y. Graphene Based Electrochemical Sensors and Biosensors: A Review. *Electroanalysis* **2010**, *22*, 1027–1036.
- (13) Stoller, M. D.; Park, S.; Zhu, Y.; An, J.; Ruoff, R. S. Graphene-Based Ultracapacitors. *Nano Lett.* **2008**, *8*, 3498–3502.
- (14) Yoo, E.; Kim, J.; Hosono, E.; Zhou, H.-s.; Kudo, T.; Honma, I. Large Reversible Li Storage of Graphene Nanosheet Families for Use in Rechargeable Lithium Ion Batteries. *Nano Lett.* **2008**, *8*, 2277–2282.
- (15) Liu, C.; Yu, Z.; Neff, D.; Zhamu, A.; Jang, B. Z. Graphene-Based Supercapacitor with an Ultrahigh Energy Density. *Nano Lett.* **2010**, *10*, 4863–4868.
- (16) Ismach, A.; Druzgalski, C.; Penwell, S.; Schwartzberg, A.; Zheng, M.; Javey, A.; Bokor, J.; Zhang, Y. G. Direct Chemical Vapor Deposition of Graphene on Dielectric Surfaces. *Nano Lett.* **2010**, *10*, 1542–1548.
- (17) Su, C. Y.; Lu, A. Y.; Wu, C. Y.; Li, Y. T.; Liu, K. K.; Zhang, W. J.; Lin, S. Y.; Juang, Z. Y.; Zhong, Y. L.; Chen, F. R.; Li, L. J. Direct Formation of Wafer Scale Graphene Thin Layers on Insulating Substrates by Chemical Vapor Deposition. *Nano Lett.* **2011**, *11*, 3612–3616.
- (18) Bi, H.; Sun, S.; Huang, F.; Xie, X.; Jiang, M. Direct Growth of Few-Layer Graphene Films on SiO₂ Substrates and Their Photovoltaic Applications. *J. Mater. Chem.* **2012**, *22*, 411–416.
- (19) Teng, P.-Y.; Lu, C.-C.; Akiyama-Hasegawa, K.; Lin, Y.-C.; Yeh, C.-H.; Suenaga, K.; Chiu, P.-W. Remote Catalyzation for Direct

Formation of Graphene Layers on Oxides. *Nano Lett.* **2012**, *12*, 1379–1384.

(20) Chen, Z.; Qi, Y.; Chen, X.; Zhang, Y.; Liu, Z. Direct CVD Growth of Graphene on Traditional Glass: Methods and Mechanisms. *Adv. Mater.* **2019**, *31*, 1803639.

(21) Bae, J. J.; Lim, S. C.; Han, G. H.; Jo, Y. W.; Doung, D. L.; Kim, E. S.; Chae, S. J.; Huy, T. Q.; Van Luan, N.; Lee, Y. H. Heat Dissipation of Transparent Graphene Defoggers. *Adv. Funct. Mater.* **2012**, *22*, 4819–4826.

(22) Sun, J.; Chen, Y.; Priyadarshi, M. K.; Chen, Z.; Bachmatiuk, A.; Zou, Z.; Chen, Z.; Song, X.; Gao, Y.; Rummeli, M. H.; Zhang, Y.; Liu, Z. Direct Chemical Vapor Deposition-Derived Graphene Glasses Targeting Wide Ranged Applications. *Nano Lett.* **2015**, *15*, 5846–5854.

(23) Wang, H.; Liu, B.; Wang, L.; Chen, X.; Chen, Z.; Qi, Y.; Cui, G.; Xie, H.; Zhang, Y.; Liu, Z. Graphene Glass Inducing Multidomain Orientations in Cholesteric Liquid Crystal Devices toward Wide Viewing Angles. *ACS Nano* **2018**, *12*, 6443–6451.

(24) Zhang, Z. P.; Zhou, F.; Yang, P. F.; Jiang, B.; Hu, J. Y.; Gao, X.; Zhang, Y. F. Direct Growth of Multi-Layer Graphene on Quartz Glass for High-Performance Broadband Neutral Density Filter Applications. *Adv. Opt. Mater.* **2020**, *8*, 2000166.

(25) Sun, J.; Chen, Y.; Cai, X.; Ma, B.; Chen, Z.; Priyadarshi, M. K.; Chen, K.; Gao, T.; Song, X.; Ji, Q.; Guo, X.; Zou, D.; Zhang, Y.; Liu, Z. Direct Low-Temperature Synthesis of Graphene on Various Glasses by Plasma-Enhanced Chemical Vapor Deposition for Versatile, Cost-Effective Electrodes. *Nano Res.* **2015**, *8*, 3496–3504.

(26) Ci, H.; Ren, H.; Qi, Y.; Chen, X.; Chen, Z.; Zhang, J.; Zhang, Y.; Liu, Z. 6-Inch Uniform Vertically-Oriented Graphene on Soda-Lime Glass for Photothermal Applications. *Nano Res.* **2018**, *11*, 3106–3115.

(27) Shang, N. G.; Papakonstantinou, P.; McMullan, M.; Chu, M.; Stamboulis, A.; Potenza, A.; Dhesi, S. S.; Marchetto, H. Catalyst-Free Efficient Growth, Orientation and Biosensing Properties of Multilayer Graphene Nanoflake Films with Sharp Edge Planes. *Adv. Funct. Mater.* **2008**, *18*, 3506–3514.

(28) Bo, Z.; Yang, Y.; Chen, J.; Yu, K.; Yan, J.; Cen, K. Plasma-Enhanced Chemical Vapor Deposition Synthesis of Vertically Oriented Graphene Nanosheets. *Nanoscale* **2013**, *5*, 5180–5204.

(29) Shan, J.; Cui, L.; Zhou, F.; Wang, R.; Cui, K.; Zhang, Y.; Liu, Z. Ethanol-Precursor-Mediated Growth and Thermochromic Applications of Highly Conductive Vertically Oriented Graphene on Soda-Lime Glass. *ACS Appl. Mater. Interfaces* **2020**, *12*, 11972–11978.

(30) Cui, L.; Huan, Y.; Shan, J.; Liu, B.; Liu, J.; Xie, H.; Zhou, F.; Gao, P.; Zhang, Y.; Liu, Z. Highly Conductive Nitrogen-Doped Vertically Oriented Graphene toward Versatile Electrode-Related Applications. *ACS Nano* **2020**, *14*, 15327–15335.

(31) Bunch, J. S.; Dunn, M. L. Adhesion Mechanics of Graphene Membranes. *Solid State Commun.* **2012**, *152*, 1359–1364.

(32) Wood, J. D.; Harvey, C. M.; Wang, S. Adhesion Toughness of Multilayer Graphene Films. *Nat. Commun.* **2017**, *8*, 1952.

(33) Lu, Z. X.; Dunn, M. L. van der Waals Adhesion of Graphene Membranes. *J. Appl. Phys.* **2010**, *107*, No. 044301.

(34) Koenig, S. P.; Boddeti, N. G.; Dunn, M. L.; Bunch, J. S. Ultrastrong Adhesion of Graphene Membranes. *Nat. Nanotechnol.* **2011**, *6*, 543–546.

(35) Liu, X.; Boddeti, N. G.; Szpunar, M. R.; Wang, L.; Rodriguez, M. A.; Long, R.; Xiao, J.; Dunn, M. L.; Bunch, J. S. Observation of Pull-In Instability in Graphene Membranes under Interfacial Forces. *Nano Lett.* **2013**, *13*, 2309–2313.

(36) Jung, W.; Park, J.; Yoon, T.; Kim, T.-S.; Kim, S.; Han, C.-S. Prevention of Water Permeation by Strong Adhesion between Graphene and SiO₂ Substrate. *Small* **2014**, *10*, 1704–1711.

(37) Das, S.; Lahiri, D.; Agarwal, A.; Choi, W. Interfacial Bonding Characteristics between Graphene and Dielectric Substrates. *Nanotechnology* **2014**, *25*, No. 045707.

(38) Gawlik, G.; Piatkowska, A.; Ciepiewski, P.; Baranowski, J. M.; Jagielski, J. Improvement of Graphene Scratch Resistance by Ion

Beam Bombardment. *Nucl. Instrum. Methods Phys. Res., Sect. B* **2020**, *474*, 10–14.

(39) Zhang, J. H.; Wang, X.; Yang, W. W.; Yu, W. D.; Feng, T.; Li, Q.; Liu, X. H.; Yang, C. R. Interaction between Carbon Nanotubes and Substrate and Its Implication on Field Emission Mechanism. *Carbon* **2006**, *44*, 418–422.

(40) Aouani, H.; Wenger, J.; Gerard, D.; Rigneault, H.; Devaux, E.; Ebbesen, T. W.; Mahdavi, F.; Xu, T.; Blair, S. Crucial Role of the Adhesion Layer on the Plasmonic Fluorescence Enhancement. *ACS Nano* **2009**, *3*, 2043–2048.

(41) Todeschini, M.; Bastos da Silva Fanta, A.; Jensen, F.; Wagner, J. B.; Han, A. Influence of Ti and Cr Adhesion Layers on Ultrathin Au Films. *ACS Appl. Mater. Interfaces* **2017**, *9*, 37374–37385.

(42) Abe, N.; Otani, Y.; Miyake, M.; Kurita, M.; Takeda, H.; Okamura, S.; Shiosaki, T. Influence of a TiO₂ Adhesion Layer on the Structure and the Orientation of a Pt Layer in Pt/TiO₂/SiO₂/Si Structures. *Jpn. J. Appl. Phys.* **2003**, *42*, 2791–2795.

(43) Cho, J. H.; Seo, Y.; Dolocan, A.; Hall, N. A.; Cullinan, M. A. Monolayer Graphene Grown on Nanoscale Pt Films Deposited on TiO₂ Substrates for Micro- and Nanoelectromechanical Systems. *ACS Appl. Nano Mater.* **2020**, *3*, 9731–9739.

(44) Hristova, E.; Arsov, L.; Popov, B. N.; White, R. E. Ellipsometric and Raman Spectroscopic Study of Thermally Formed Films on Titanium. *J. Electrochem. Soc.* **1997**, *144*, 2318–2323.

(45) Zhang, Y.; Fang, Z. G. Z.; Xu, L.; Sun, P.; Van Devener, B.; Zheng, S. L.; Xia, Y.; Li, P.; Zhang, Y. Mitigation of the Surface Oxidation of Titanium by Hydrogen. *J. Phys. Chem. C* **2018**, *122*, 20691–20700.

(46) Noda, H.; Oikawa, K.; Ogata, T.; Matsuki, K.; Kamada, H. Preparation of Titanium (IV) Oxides and Its Characterization. *Nippon Kagaku Kaishi* **1986**, 1084–1090.

(47) Zhang, L.; Shi, Z.; Wang, Y.; Yang, R.; Shi, D.; Zhang, G. Catalyst-Free Growth of Nanographene Films on Various Substrates. *Nano Res.* **2011**, *4*, 315–321.

(48) Huang, K.; Li, Y.; Xing, Y. Carbothermal Synthesis of Titanium Oxycarbide As Electrocatalyst Support with High Oxygen Evolution Reaction Activity. *J. Mater. Res.* **2013**, *28*, 454–460.

(49) Hahn, R.; Schmidt-Stein, F.; Salonen, J.; Thiemann, S.; Song, Y. Y.; Kunze, J.; Lehto, V. P.; Schmuki, P. Semimetallic TiO₂ Nanotubes. *Angew. Chem., Int. Ed.* **2009**, *48*, 7236–7239.

(50) Ma, Y.; Jang, H.; Kim, S. J.; Pang, C.; Chae, H. Copper-Assisted Direct Growth of Vertical Graphene Nanosheets on Glass Substrates by Low-Temperature Plasma-Enhanced Chemical Vapour Deposition Process. *Nanoscale Res. Lett.* **2015**, *10*, 308.

(51) Chen, X. D.; Chen, Z. L.; Jiang, W. S.; Zhang, C. H.; Sun, J. Y.; Wang, H. H.; Xin, W.; Lin, L.; Priyadarshi, M. K.; Yang, H.; Liu, Z. B.; Tian, J. G.; Zhang, Y. Y.; Zhang, Y. F.; Liu, Z. F. Fast Growth and Broad Applications of 25-Inch Uniform Graphene Glass. *Adv. Mater.* **2017**, *29*, 1603428.

(52) Cemin, F.; Bim, L. T.; Leidens, L. M.; Morales, M.; Baumvol, I. J. R.; Alvarez, F.; Figueroa, C. A. Identification of the Chemical Bonding Prompting Adhesion of a-C:H Thin Films on Ferrous Alloy Intermediated by a SiC_x:H Buffer Layer. *ACS Appl. Mater. Interfaces* **2015**, *7*, 15909–15917.

(53) Gatzert, C.; Mack, D. E.; Guillon, O.; Vassen, R. Improved Adhesion of Different Environmental Barrier Coatings on Al₂O₃/Al₂O₃-Ceramic Matrix Composites. *Adv. Eng. Mater.* **2020**, *22*, 2000087.

(54) Chen, J.; Wen, Y.; Guo, Y.; Wu, B.; Huang, L.; Xue, Y.; Geng, D.; Wang, D.; Yu, G.; Liu, Y. Oxygen-Aided Synthesis of Polycrystalline Graphene on Silicon Dioxide Substrates. *J. Am. Chem. Soc.* **2011**, *133*, 17548–17551.

(55) Chen, Z.; Guan, B.; Chen, X.-D.; Zeng, Q.; Lin, L.; Wang, R.; Priyadarshi, M. K.; Sun, J.; Zhang, Z.; Wei, T.; Li, J.; Zhang, Y.; Zhang, Y.; Liu, Z. Fast and Uniform Growth of Graphene Glass Using Confined-Flow Chemical Vapor Deposition and Its Unique Applications. *Nano Res.* **2016**, *9*, 3048–3055.

(56) Tsai, P. C.; Hwang, Y. F.; Chiang, J. Y.; Chen, W. J. The Effects of Deposition Parameters on the Structure and Properties of

Titanium-Containing DLC Films Synthesized by Cathodic Arc Plasma Evaporation. *Surf. Coat. Technol.* **2008**, *202*, 5350–5355.

(57) Blackstock, J. J.; Donley, C. L.; Stickle, W. F.; Ohlberg, D. A. A.; Yang, J. J.; Stewart, D. R.; Williams, R. S. Oxide and Carbide Formation at Titanium/Organic Monolayer Interfaces. *J. Am. Chem. Soc.* **2008**, *130*, 4041–4047.

(58) Hamasha, M. M.; Dhakal, T.; Alzoubi, K.; Albahri, S.; Qasaimeh, A.; Lu, S. S.; Westgate, C. R. Stability of ITO Thin Film on Flexible Substrate under Thermal Aging and Thermal Cycling Conditions. *J. Disp. Technol.* **2012**, *8*, 385–390.